Supporting Information

Hydrogen Peroxide Generation with 100% Faradaic Efficiency on Metal-Free Carbon Black

Zhe Wang,[†] Qin-Kun Li,[‡] Chenhao Zhang,[†] Zhihua Cheng,[†] Weiyin Chen,[†] Emily A. McHugh,[†] Robert A. Carter,[†] Boris I. Yakobson,[‡, §] and James M. Tour[†, ‡, §*]*

[†]Department of Chemistry, [‡]Department of Materials Science and NanoEngineering, [§]Smalley-Curl Institute, NanoCarbon Center and the Welch Institute for Advanced Materials, Rice University, 6100 Main Street, Houston, TX 77005, USA

E-mail: biy@rice.edu (Boris Yakobson), tour@rice.edu (James Tour)

Experimental/Methods

Electrochemically active surface area (ECSA)

ECSA is calculated from the electrochemical double-layer capacitance (C_{dl}) of the catalyst.[1] C_{dl} was determined from the slope by plotting current density as a function of scan rate in a potential range where no Faradaic current was generated. The results were shown in Figure S11 and Table S5. The ECSA was calculated from the following equation:

$$\mathrm{ECSA} = \frac{C_{dl}}{C_s}$$

where C_s is the specific capacitance of a flat standard electrode with 1 cm^2 of real surface area. The value of C_s is determined to be 40 μF cm^{-2} according to several previous studies.[1,2] The calculated results are listed in Table S5.

Calibration of reference electrodes

The HgO/Hg (1 M KOH) and AgCl/Ag (saturated KCl) reference electrodes used were both calibrated with respect to the reversible hydrogen electrode (RHE).

$$E(RHE) = E(HgO/Hg) + 0.900\ V$$

$$E(RHE) = E(AgCl/Ag) + 0.970\ V$$

Koutecky-Levich plot

The O_2 reduction current satisfies Koutecky-Levich (K-L) equation,

$$J^{-1}=J_K^{-1}+J_L^{-1}$$

where J_K is the potential dependent kinetic current and J_L is the Levich current,

$$J_L=0.62nF[O_2](D_{O2})^{2/3}\omega^{1/2}\nu^{-1/6}$$

where n is the electron transfer number, $[O_2]$ is the concentration of O_2 in a saturated solution (1.26 mol m^{-3}) at 25 °C, D_{O2} is the diffusion coefficient of O_2 (1.93×10^{-5} cm^2 s^{-1}), ω is the angular velocity of the disc and ν is the kinematic viscosity of the solution (0.01 cm^2 s^{-1}) at 25 °C.[3]

Preparation of CB-UV: A thin layer of commercial CB (black pearl 2000, Cabot) was scattered uniformly onto a microscope glass slide, which was then transferred into a UV-ozone cleaner (Boekel Model 135500) and treated in the ozone environment for 1 h.

Preparation of CB-Plasma: A thin layer of commercial CB (black pearl 2000, Cabot) was uniformly scattered onto a microscope glass slide, which was placed in a home-made boat and transferred into a plasma cleaner (Model 1020, Fischione Instruments) and treated with plasma under 20% O_2/Ar atmosphere.

Preparation of CB-A: CB-Plasma powders were scattered in a boat, which was then transferred into a quartz tube and heated to 750 °C with a heating rate of 10 °C min^{-1} and maintained at 750 °C for 2 h under 150 sccm Ar flow.

Characterization: TEM, scanning TEM (STEM) and energy-dispersive spectroscopy (EDS) images were acquired on a JEOL-2100F field emission gun transmission electron microscope at 200 kV acceleration voltage. X-ray photoelectron spectroscopies (XPS) of the samples were investigated on a PHI Quantera scanning X-ray microprobe at 4×10^{-9} Torr. Elemental spectra were shifted by calibrating the obtained C1s peaks to 284.6 eV. XRD patterns were collected on a Rigaku D/Max Ultima II (Rigaku Corporation), which is equipped with a Cu Kα radiation, a graphite monochrometer, and a scintillation counter. Raman spectra were obtained on a Renishaw Raman microscope with a 532 nm laser. The BET characterizations were done on a Quantachrome Autosorb-iQ3-MP/Kr BET surface analyzer. UV-Vis spectra were performed on a SHIMADZU UV-3600Plus configured with a photomultiplier tube from 200 to 400 nm wavelength. ICP-MS trace-metal elemental analysis was performed using a Perkin Elmer Nexion 300 inductively coupled plasma mass spectrometer equipped with a quadrupole mass analyzer.

TEM of the same carbon materials before and after oxidation: TEM grids with labels were carefully mixed with CB powders and shaken for 3 min. The as-prepared TEM grids were then loaded into the TEM holder and a set of marked areas checked under TEM. Afterward, the grids along with the holder were treated with O_2 plasma for 15 s or treated with UV Ozone for 60 s to mimic the sample preparation process while avoiding destroying the grids. The same area was then checked under TEM again and compared with the images taken before the oxidizing treatments.

Electrochemical Measurements: Rotating disk electrode (RDE) and rotating ring-disk electrode (RRDE) tests were performed in an electrochemical cell. Rotating rate was controlled with a Pine

Instrument rotator (model: AFMSRCE). Typically, the catalyst (1.0 mg) and 5 wt% Nafion solution (80 μL) were mixed in 1.60 mL ethanol and 6.40 mL water followed by 4 h bath sonication (Cole Parmer, model 08849–00) to obtain a homogeneous ink. 16.00 μL as-prepared catalyst ink was loaded onto a RDE (glassy carbon, 5 mm in diameter) and dried in air at room temperature. RDE electrochemical tests were carried out using a CHI 608D electrochemical workstation (CH Instruments, Inc.) with a three-electrode configuration. A graphite rod and a HgO/Hg (1 M KOH) electrode are used as the counter electrode and reference electrode, respectively. The ORR tests were conducted in 0.1 M KOH solution with continuous O_2 bubbling to ensure the O_2 saturation. Controlled experiments in Ar atmosphere were done under the same conditions by replacing O_2 bubbling with Ar bubbling. RRDE tests were done by combining a CHI 608D electrochemical workstation (CH Instruments, Inc.) with a CS310 electrochemical workstation (Wuhan Corrtest Instruments Corp., Ltd.). The disk electrode was scanned at a rate of 10 mV/s and the ring potential was kept constant at (1.16 ± 0.01) V *vs* RHE using a chronoamperometry method. The H_2O_2 yield and electron transfer number were calculated using the following eq 1 and 2:

$$H_2O_2\% = \frac{I_r/N}{I_r/N+I_d} \times 200\% \quad (1)$$

$$n = 4 \times \frac{I_d}{I_r/N+I_d} \quad (2)$$

Where I_d is the disk current, I_r is the ring current and N is the collection efficiency (0.25).

Bulk electrolysis was conducted in an H-cell. Typically, 8.0 mg CB-Plasma and 5 wt% Nafion solution (80 μL) were mixed in 8.00 mL solvent (water:ethanol = 4:1, v:v) and sonicated for 4 h (Cole Parmer, model 08849–00) to obtain a homogeneous ink. 0.50 mL as-prepared ink was then loaded onto a carbon paper electrode (0.5 × 1 cm^2, Toray Paper 060, Fuel Cell Store), which was left dry at room temperature overnight. H_2O_2 concentration was quantified by a cerium sulfate titration method. The yellow Ce^{4+} ion is reduced by H_2O_2 to colorless Ce^{3+} as in eq 3:

$$2Ce^{4+} + H_2O_2 \rightarrow 2Ce^{3+} + O_2 + 2H^+ \quad (3)$$

The amount of H_2O_2 is then determined by measuring the amount changing of Ce^{4+} in eq 4:

$$n_{H_2O_2} = 2\Delta n_{Ce^{4+}} \quad (4)$$

Computational Details: Spin-polarized DFT calculations are implemented in Vienna *Ab Initio* Simulation Package (VASP).[4,5] The exchange-correlation potential is described by Perdew-Burke-Ernzerhof (PBE) functional with generalized gradient approximation (GGA).[6] The projector augmented wave (PAW) method is applied to describe the electron-ion interaction[7,8] and the plane-wave energy cutoff is 500 eV. The energy and forces convergence criterion are 1×10^{-5} eV and 0.01 eV/Å, respectively. The vacuum spacing is set to 18 Å along the non-periodic direction to prevent interaction between two neighboring surfaces. The van der Waals interaction is considered by DFT-D3 method proposed by Grimme *et al*.[9]

For each step along the ORR $2e^-$ and $4e^-$ pathways, the Gibbs free energy ΔG is calculated using the computational hydrogen electrode (CHE) model developed by Norskov *et al*[10 11] and defined as the difference between free energies of the initial and final states in eq 5:[12,13]

$$\Delta G = \Delta E + \Delta ZPE - T\Delta S + \Delta G_U \quad (5)$$

where ΔE is the reaction energy obtained from DFT calculations; ΔZPE and ΔS are the zero-point energy and entropy contribution estimated by harmonic approximations due to the reaction; The bias effect on the free energy is taken into account by shifting the energy of the state by ΔG_U = - neU, where U is the electrode applied potential relative to RHE and n is the number of proton-electron pairs transferred in each step.

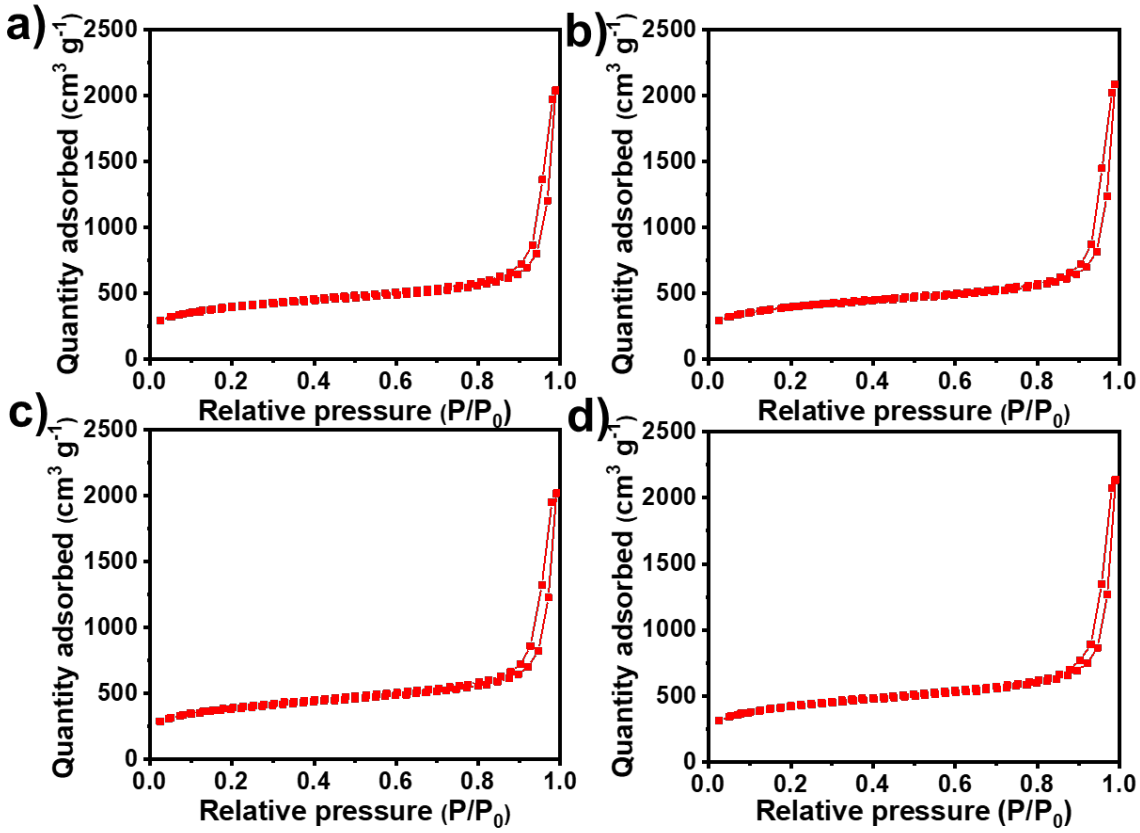

Figure S1. N_2 adsorption/desorption plots of (a) pristine CB, (b) CB-Plasma, (c) CB-UV, and (d) CB-A.

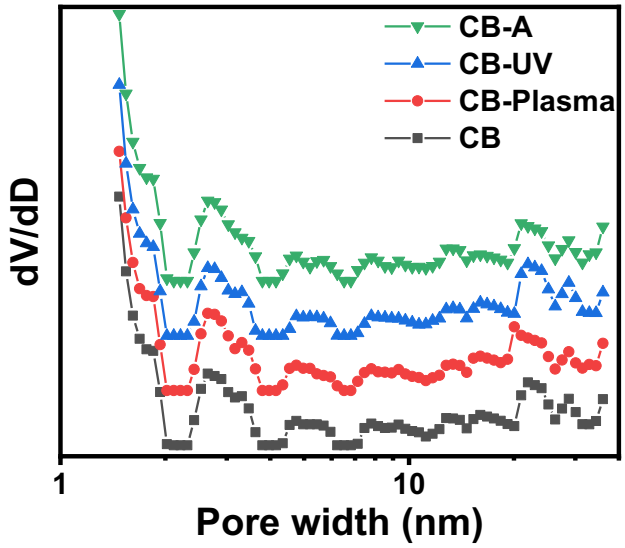

Figure S2. Pore size distributions of pristine CB, CB-Plasma, CB-UV, and CB-A.

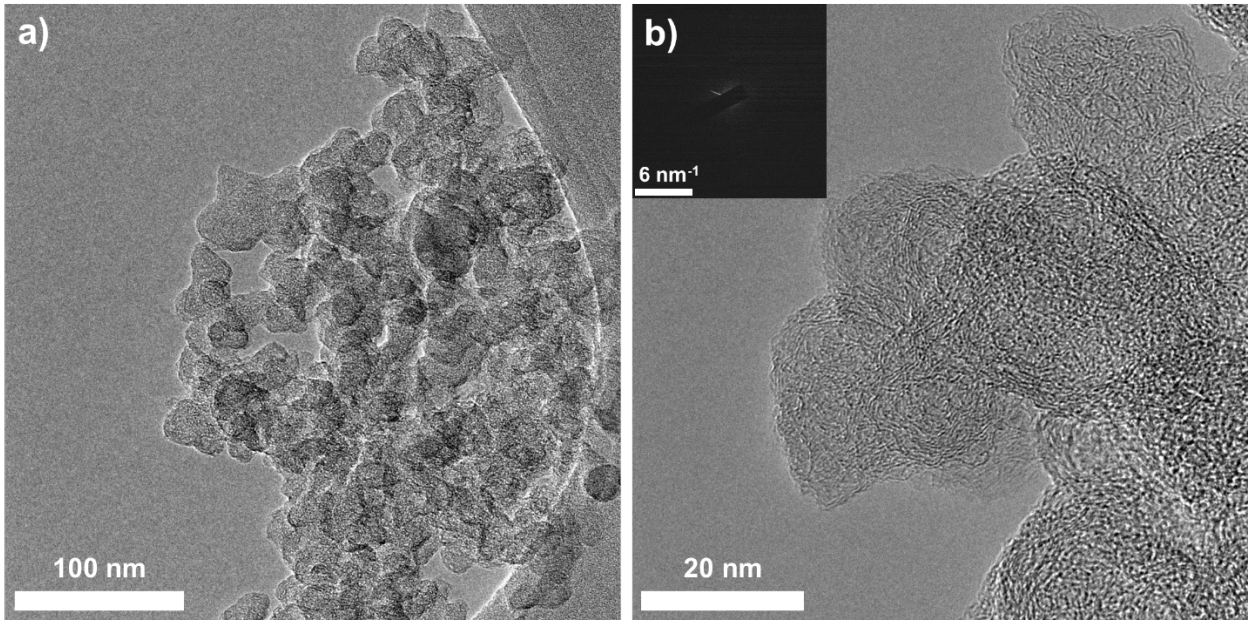

Figure S3. (a) TEM and (b) HR-TEM images of pristine CB. Inset: corresponding SAED pattern. There were no obvious lattice fringes in the HR-TEM image and only blurred rings were found in the inset SAED pattern, both of which confirm the amorphous nature of pristine CB.

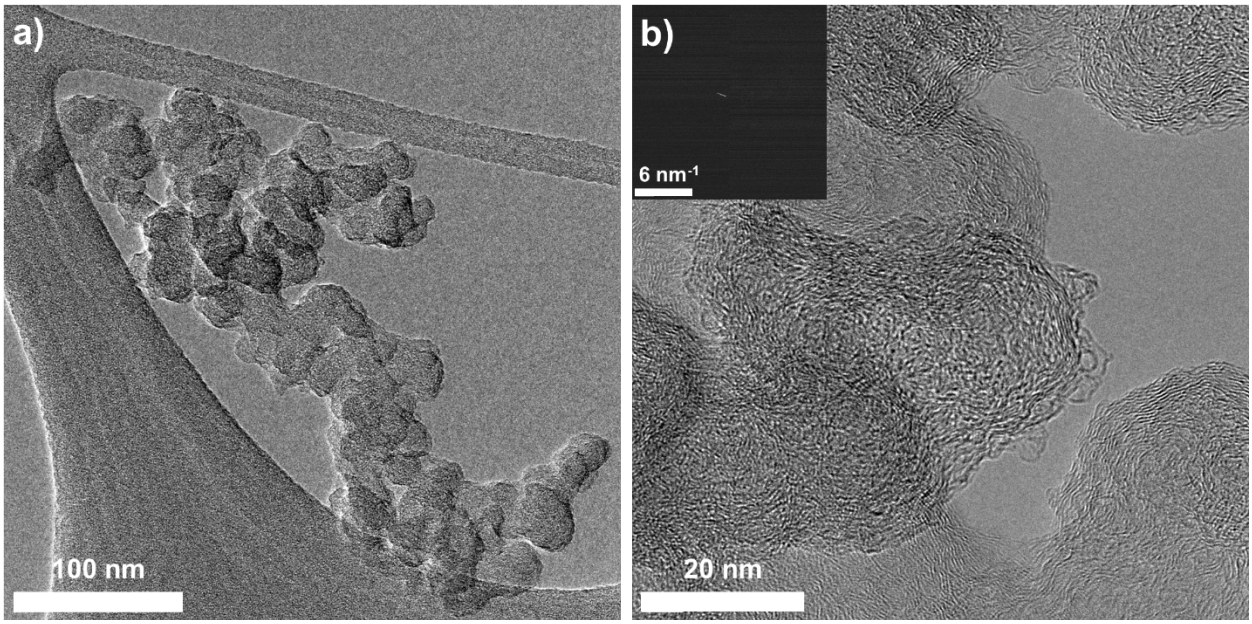

Figure S4. (a) TEM and (b) HR-TEM images of CB-Plasma. Inset: corresponding SAED pattern. There were no obvious lattice fringes in the HR-TEM image and only blurred rings were found in the inset SAED pattern, both of which confirmed the amorphous nature was maintained after plasma treatment.

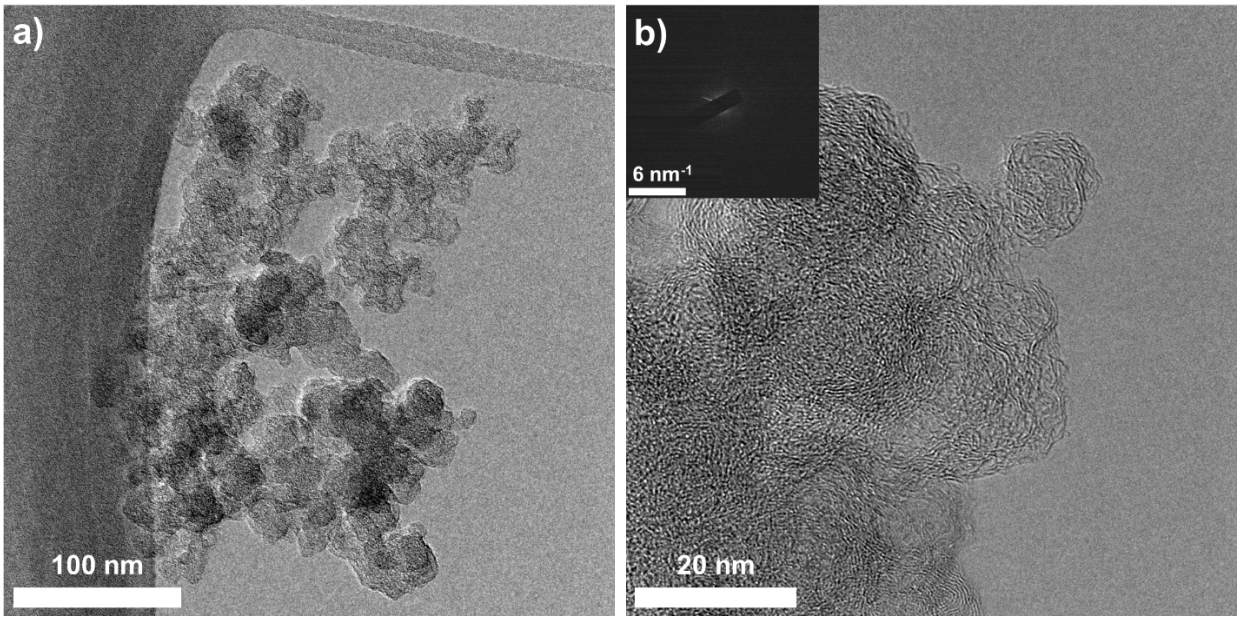

Figure S5. (a) TEM and (b) HR-TEM images of CB-UV. Inset: corresponding SAED pattern. There were no obvious lattice fringes in the HR-TEM image and only blurred rings were found in the inset SAED pattern, both of which confirmed the amorphous nature was maintained after UV-ozone treatment.

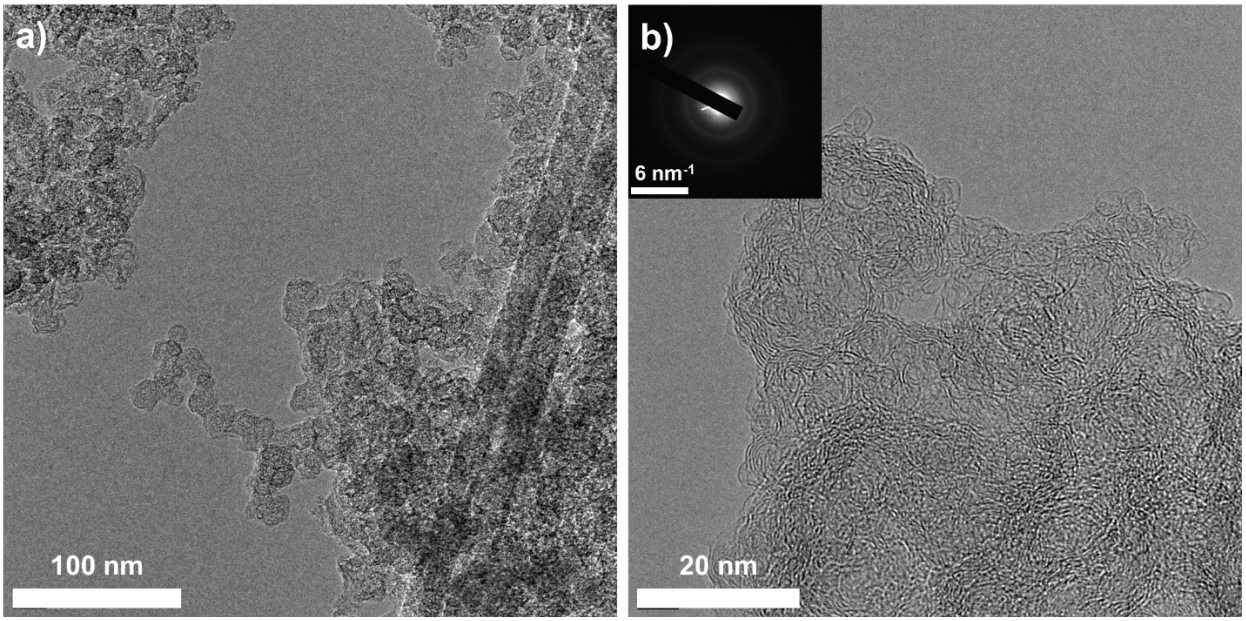

Figure S6. (a) TEM and (b) HR-TEM images of CB-A. Inset: corresponding SAED pattern. There were no obvious lattice fringes in the HR-TEM image and only blurred rings were found in the inset SAED pattern, both of which confirmed the amorphous nature was maintained after the high-temperature annealing process.

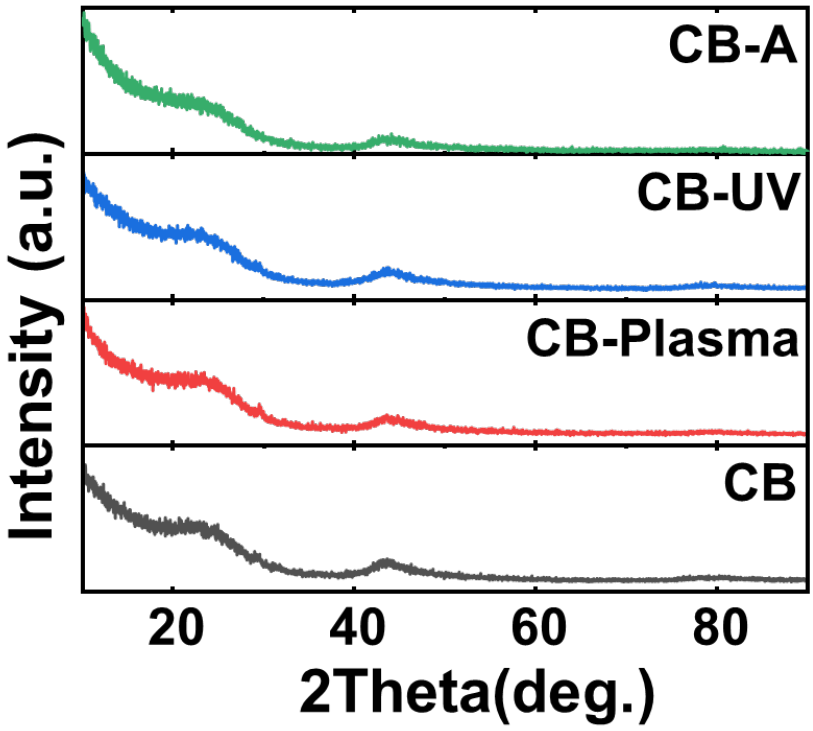

Figure S7. XRD patterns of CB-A, CB-UV, CB-Plasma, and CB-A. Only broad peaks were observed, confirming the amorphous nature of all the samples.

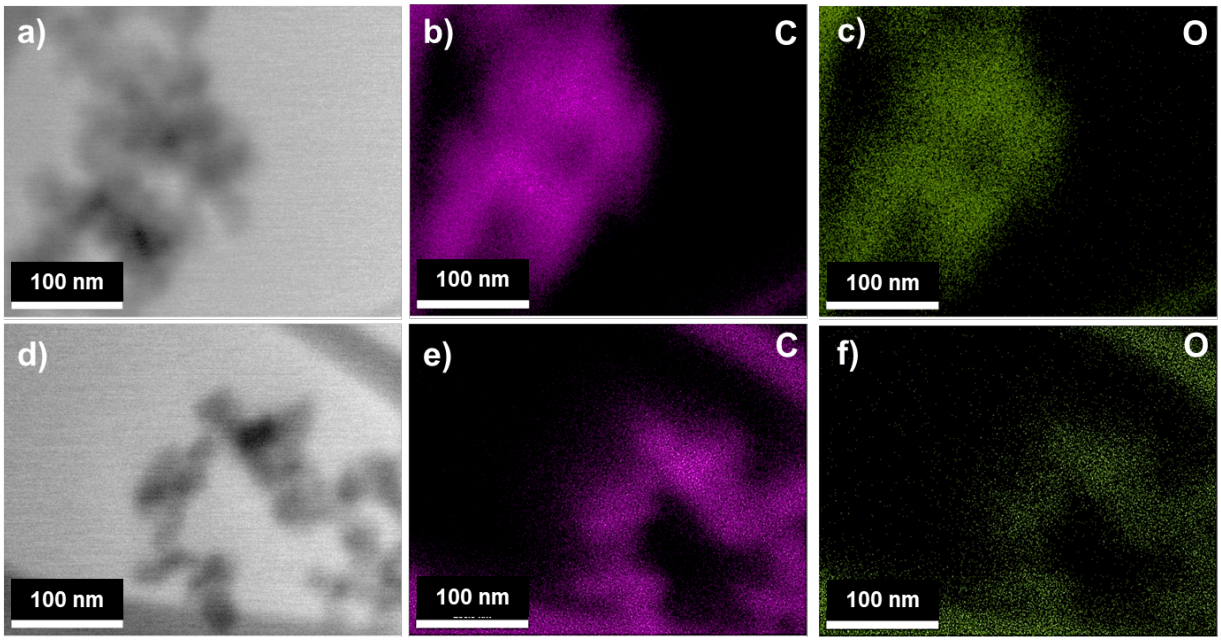

Figure S8. (a) STEM image of CB-UV on a lacey carbon TEM grid and (b-c) respective elemental distribution of C and O. Purple: carbon; green: oxygen. (d) STEM image of CB-Plasma on a lacey carbon TEM grid and (e-f) respective elemental distribution of C and O. Purple: carbon; green: oxygen. Oxygen is uniformly distributed in both samples.

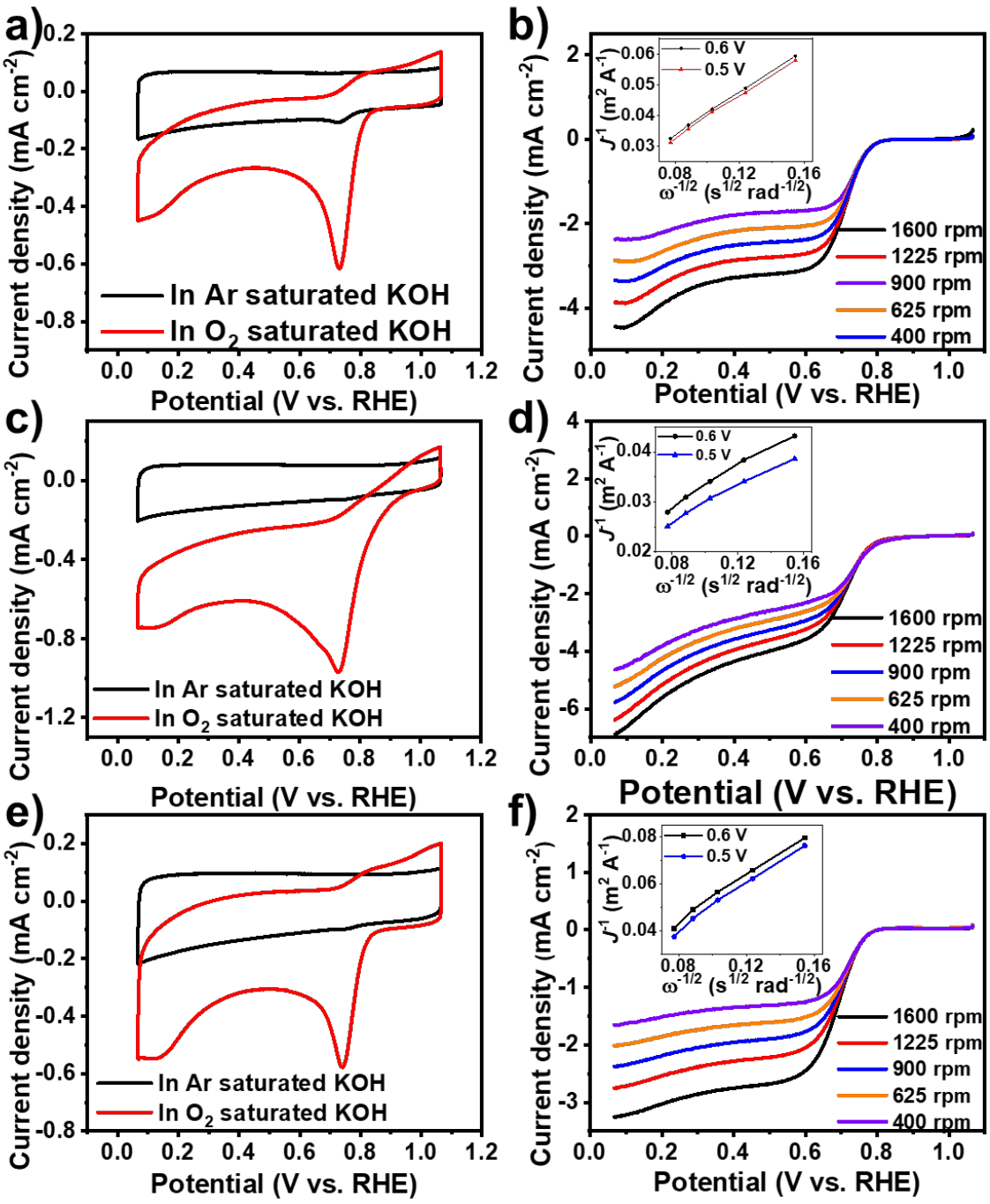

Figure S9. CV curves in Ar- and O_2-saturated 0.1 M KOH of (a) CB, (c) CB-UV, and (e) CB-A. Scan rate: 10 mV s^{-1}. LSV curves at different rotating speeds ranging from 400 rpm to 1600 rpm of (b) CB, (d) CB-UV, and (f) CB-A. Insets: corresponding K-L plots at different potentials. Calculated electron transfer numbers of CB, CB-UV, and CB-A are 2.3, 2.3, and 2.0, respectively.

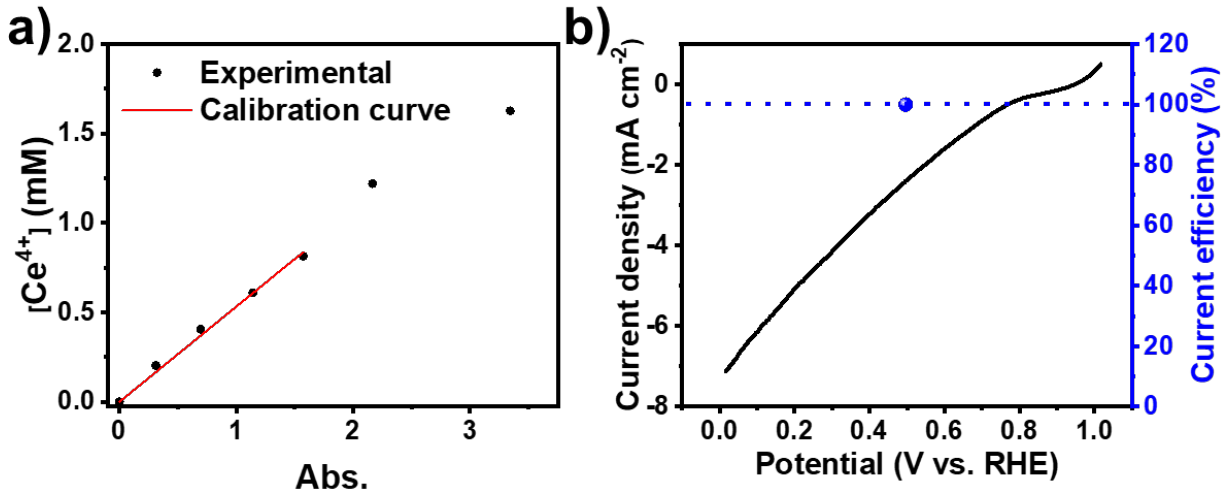

Figure S10. (a) Calibration curve of Ce^{4+} concentration and absorbance at 319 nm. (b) Polarization curve on carbon paper electrode in O_2 saturated 0.1 M KOH electrolyte and calculated current efficiency of bulk electrolysis determined by $Ce(SO_4)_2$ titration method.

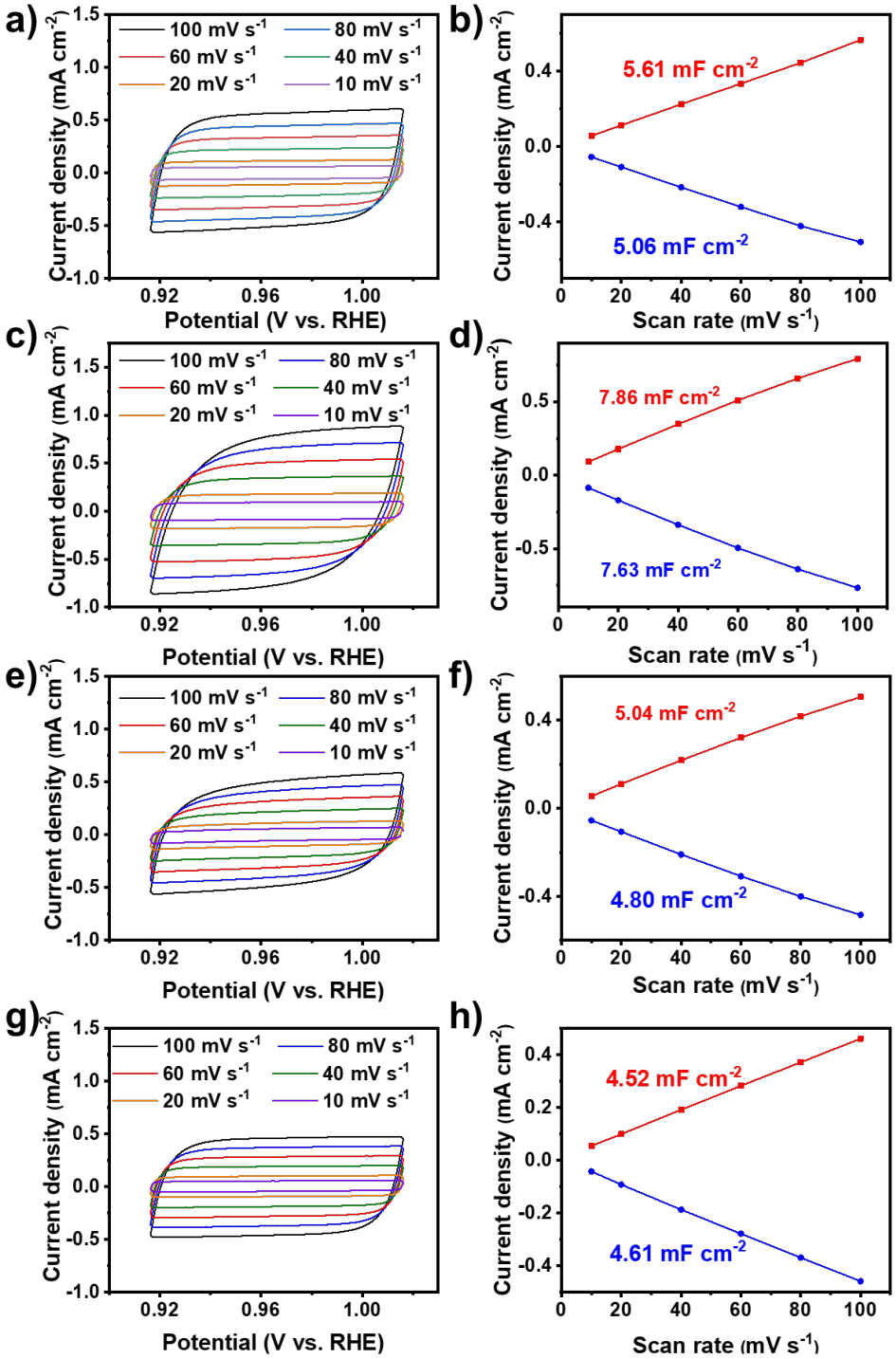

Figure S11. Determination of the C_{dl}. CV curves recorded at 10, 20, 40, 60, 80, 100 mV s^{-1} of (a) CB, (c) CB-Plasma, (e) CB-UV, (g) CB-A. Current density at 0.96 V (*vs* RHE) as a function of scan rate along with the linear fitting curves of (b) CB, (d) CB-Plasma, (f) CB-UV, (h) CB-A are shown.

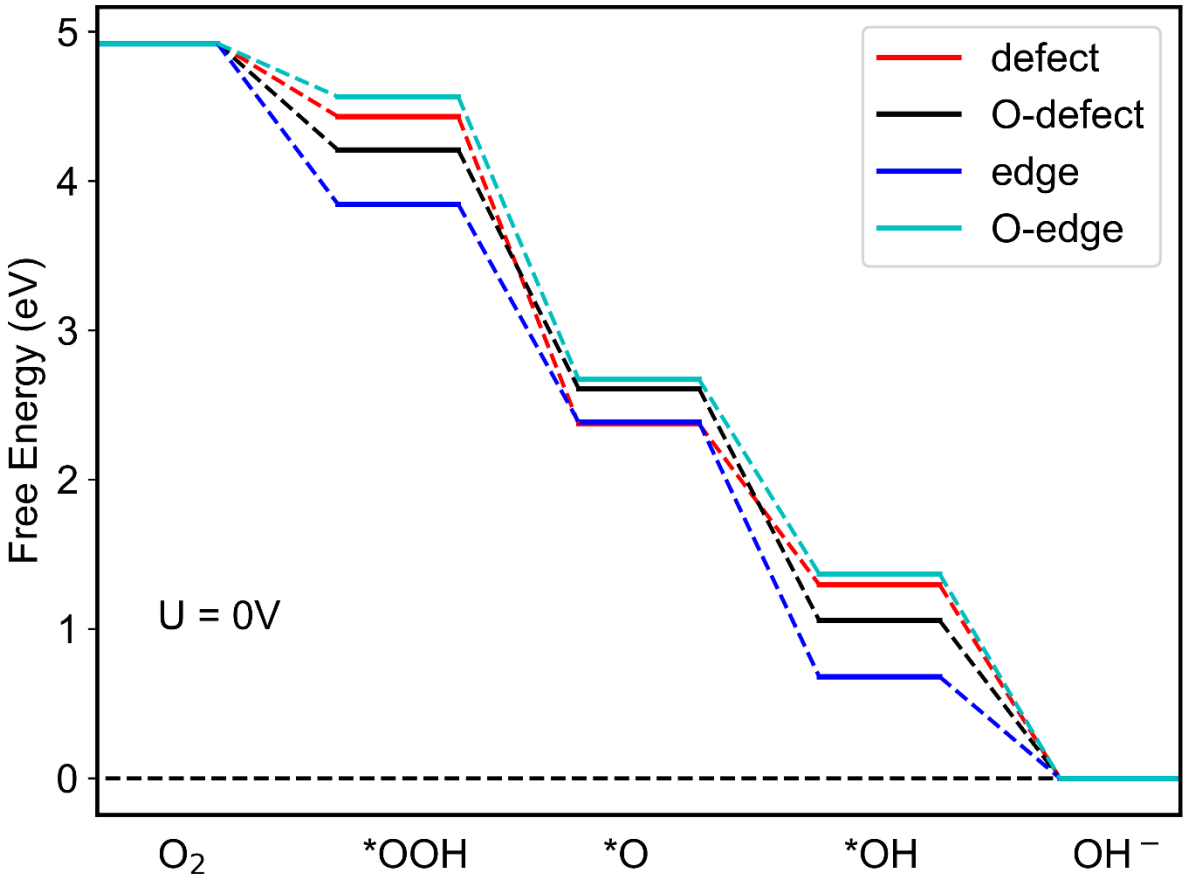

Figure S12. Free energy profile of $4e^-$ pathway at U = 0 V on four defect GNR models.

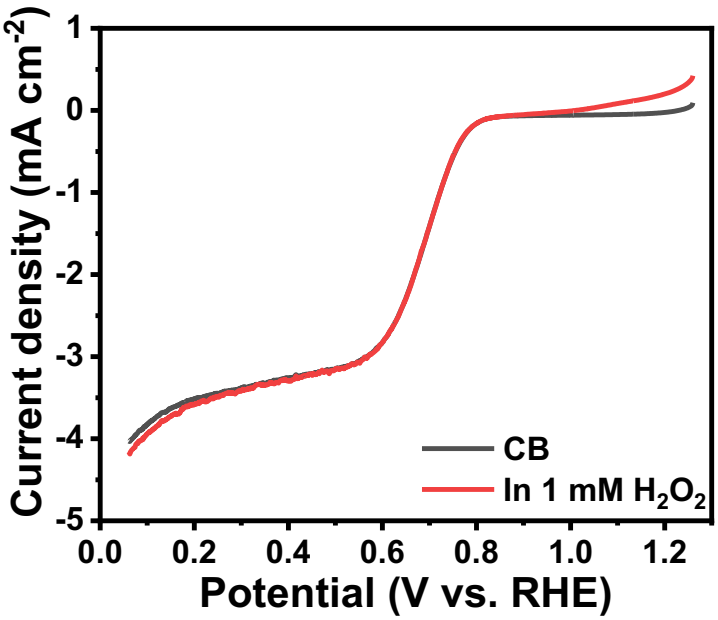

Figure S13. LSV curves of CB in O_2-saturated 0.1 M KOH and O_2-saturated 0.1 M KOH with 1 mM H_2O_2 at a rotating speed of 1600 rpm. The current differences above 0.8 V and below 0.3 V are attributed to H_2O_2 oxidation current and to H_2O_2 reduction current, respectively. Scan rate: 20 mV s^{-1}.

Table S1. Brunauer-Emmett-Teller (BET) Surface Analysis Results

Sample	Specific surface area (m^2 g^{-1})	Pore Width (nm)
CB	1307	1.47
CB-UV	1312	1.47
CB-Plasma	1281	1.47
CB-A	1392	1.47

Table S2. Elemental Composition of CB, CB-Plasma, CB-UV, and CB-A from XPS

Sample	C (at%)	O (at%)
CB	99.2	0.8
CB-Plasma	76.5	23.5
CB-UV	91.5	8.5
CB-A	98.4	1.6

Table S3. Concentrations of Carbon Species from XPS in CB, CB-Plasma, CB-UV, and CB-A

Sample	C-C/C=C (at%)	C-O (at%)	C=O (at%)	O=C-O (at%)
CB	100.0	<0.1	<0.1	<0.1
CB-Plasma	81.6	4.8	4.9	8.8
CB-UV	88.4	4.8	2.9	3.9
CB-A	100.0	<0.1	<0.1	<0.1

Table S4. Concentrations of oxygen species from XPS in CB-Plasma, and CB-UV

Sample	C-O (at%)	C=O (at%)
CB-Plasma	57.4	42.6
CB-UV	56.7	43.3

Table S5. C_{dl} and corresponding ECSA of CB, CB-Plasma, CB-UV, and CB-A

Sample	C_{dl} (mF cm^{-2})	ECSA (cm^2 $cm^{-2}_{electrode}$)
CB	5.34	133
CB-Plasma	7.75	194
CB-UV	4.92	123
CB-A	4.57	114

References

1. Zhang, C.; Sha, J.; Fei, H.; Liu, M.; Yazdi, S.; Zhang, J.; Zhong, Q.; Zou, X.; Zhao, N.; Yu, H.; Jiang, Z.; Ringe, E.; Yakobson, B. I.; Dong, J.; Chen, D.; Tour, J. M. Single-Atomic Ruthenium Catalytic Sites on Nitrogen-Doped Graphene for Oxygen Reduction Reaction in Acidic Medium. *ACS Nano* **2017**, *11*, 6930.

2. a) McCrory, C. C.; Jung, S.; Peters, J. C.; Jaramillo, T. F. Benchmarking Heterogeneous Electrocatalysts for the Oxygen Evolution Reaction. *J. Am. Chem. Soc.* **2013**, *135*, 16977; b) Zhang, J.; Ren, M.; Wang, L.; Li, Y.; Yakobson, B. I.; Tour, J. M. Oxidized Laser-Induced Graphene for Efficient Oxygen Electrocatalysis. *Adv. Mater.* **2018**, *30*, 1707319.

3. Guo, Y.; Yuan, P.; Zhang, J.; Hu, Y.; Amiinu, I. S.; Wang, X.; Zhou, J.; Xia, H.; Song, Z.; Xu, Q.; Mu, S. Carbon Nanosheets Containing Discrete Co-N_x-B_y-C Active Sites for Efficient Oxygen Electrocatalysis and Rechargeable Zn–Air Batteries. *ACS Nano* **2018**, *12*, 1894-1901.

4. Kresse, G.; Furthmüller, J. Efficiency of *Ab-Initio* Total Energy Calculations for Metals and Semiconductors using a Plane-Wave Basis Set. *Comput. Mater. Sci.* **1996,** *6*, 15-50.

5. Kresse, G.; Furthmüller, J. Efficient Iterative Schemes for *Ab Initio* Total-Energy Calculations Using a Plane-Wave Basis Set. *Phys. Rev. B* **1996,** *54*, 11169.

6. Perdew, J. P.; Burke, K.; Ernzerhof, M. Generalized Gradient Approximation Made Simple. *Phys. Rev. Lett.* **1996,** *77*, 3865.

7. Blochl, P. E. Projector Augmented-Wave Method. *Phys. Rev. B* **1994,** *50*, 17953-17979.

8. Kresse, G.; Joubert, D. From Ultrasoft Pseudopotentials to the Projector Augmented-Wave Method. *Phys. Rev. B* **1999,** *59*, 1758.

9. Grimme, S.; Antony, J.; Ehrlich, S.; Krieg, H. A Consistent and Accurate *Ab Initio* Parametrization of Density Functional Dispersion Correction (DFT-D) for the 94 Elements H-Pu. *J. Chem. Phys.* **2010,** *132*, 154104.

10. Rossmeisl, J.; Logadottir, A.; Nørskov, J. K. Electrolysis of Water on (Oxidized) Metal Surfaces. *Chem. Phys.* **2005,** *319*, 178-184.

11. Nørskov, J. K.; Rossmeisl, J.; Logadottir, A.; Lindqvist, L.; Kitchin, J. R.; Bligaard, T.; Jonsson, H. Origin of the Overpotential for Oxygen Reduction at a Fuel-Cell Cathode. *J. Phys. Chem. B* **2004,** *108*, 17886-17892.

12. Xu, H.; Cheng, D.; Cao, D.; Zeng, X. C. A Universal Principle for a Rational Design of Single-Atom Electrocatalysts. *Nat. Catal.* **2018,** *1*, 339-348.

13. Liu, S.; Li, Z.; Wang, C.; Tao, W.; Huang, M.; Zuo, M.; Yang, Y.; Yang, K.; Zhang, L.; Chen, S.; Xu, P.; Chen, Q. Turning Main-Group Element Magnesium into a Highly Active Electrocatalyst for Oxygen Reduction Reaction. *Nat. Commun.* **2020,** *11*, 938.